Determining Epicardial Surface Motion Using Elastic Registration: Towards Virtual Reality Guidance of Minimally Invasive Cardiac Interventions

Marcin Wierzbicki[1,2] and Terry M. Peters[1,2]

[1] Imaging Research Laboratories, Robarts Research Institute,
London, Ontario N6A 5K8, Canada
[2] Department of Medical Biophysics, The University of Western Ontario,
London, Ontario N6A 5C1, Canada
{mwierz, tpeters}@imaging.robarts.ca

Abstract. Minimally invasive cardiac surgery is performed on the beating heart, through inter-costal ports. The two major limitations of these procedures are: selecting port locations for optimal target coverage (based on chest x-rays and angiograms), and navigating surgical tools through a dynamic and confined environment using a 2D endoscope. To supplement the current surgery planning and guidance strategies, we continue developing VCSP – a virtual reality, patient-specific, thoracic cavity model derived from 3D pre-procedural images. In this work, we apply elastic image registration to 4D images of the heart to model the epicardial surface over the cardiac cycle. We validated our registration algorithm on CT images of a dynamic cardiac phantom and of normal canine hearts, and found the error to be 1.14 ± 0.31 mm and 0.61 ± 0.12 mm, respectively. We believe this method of modeling the epicardial surface is sufficiently accurate to be applied in cardiac surgery planning and guidance.

1 Introduction

Coronary artery disease (CAD) is the single leading cause of death in the developed world. Traditionally, CAD is treated with coronary bypass surgery through a median sternotomy under cardiopulmonary bypass. Eliminating the heart-lung machine and using a less invasive thoracotomy have been shown to reduce hospital stays and costs [1]. Such promising results have prompted the development of endoscopically-aided, port-access, bypass surgeries [2]. In spite of the sophistication of some robotic systems used to perform these interventions, critical tasks such as surgery planning and guidance are performed entirely with 2D images. Port placement is based on 2D angiography and chest x-rays, while the entire procedure is guided solely through a 2D video endoscope with a small field of view and reversed video picture. The lack of 3D surgery planning and guidance can lead to improper patient selection, sub-optimal port placement, longer procedures, and increased risks to the patient [3].

To address these issues, we have developed the Virtual Cardiac Surgery Planning platform (VCSP) [3]. In this prototype software, a model of the thoracic cavity, derived from segmented pre-procedural 3D images, is shown stereoscopically to the user, who can then optimize locations of the inter-costal ports interactively. To adapt

R.E. Ellis and T.M. Peters (Eds.): MICCAI 2003, LNCS 2878, pp. 722–729, 2003.

VCSP from surgery planning to guidance, we plan to update the environment with intra-operative ultrasound (US) images, similar to the approach proposed for neurosurgery in [4]. Currently, the patient's chest wall and ribs are represented in the VCSP prototype. A non-patient specific dynamic model of the coronary arteries derived from 2D angiograms is also available [5]. The aim of this work is to continue developing VCSP by including patient-specific, high resolution, dynamic models of the epicardial surface, that will serve as a basis with which models of the coronary arteries and other structures of interest will be merged

Previous work in cardiac modeling has concentrated primarily on analyzing the left-ventricle (LV) - the structure most important for function. An exception is the work by Sørensen *et al.* [6], who used image segmentation to create a static 3D model of the entire heart from magnetic resonance (MR) images at end-diastole. Others have employed segmentation of cardiac images to visualize various structures [7]. Although effective on single 3D images, these methods fail to take advantage of the correspondence of adjacent time points in a 4D dataset. In contrast, the work by Declerc *et al.* [8] makes use of the correspondence between time frames, but only for the LV, where the geometry can be simplified to minimize the amount of parameters describing the motion. Another method of deriving motion from a temporal image sequence is through voxel-based, elastic image registration. Motion information obtained by registering image time frames together can be used to propagate a static model (created using a single segmentation) through the cardiac cycle. Similar ideas have been used to compensate for motion blur in PET images [9], and to segment the myocardium, LV and RV from 4D MR images [10]. Voxel-based methods are convenient for planning and guidance of minimally invasive cardiac surgeries, since the amount of user variability and the time required per patient is minimal.

In this paper we validate our elastic registration algorithm applied to the problem of accurately representing a dynamic epicardial surface. We assert the performance of our algorithm with computed tomography (CT) images obtained from a dynamic cardiac phantom by following easily identifiable landmarks, and with images of normal canine subjects, where we used consistency measures to estimate the error in epicardial surface location. Multi-slice helical CT images were used because of the superior voxel size (~ 0.15 mm^3), but comparable time resolution (100 msec) to MR. Ultimately, the epicardial surface model will be merged with models of much smaller structures, such as the coronary arteries. Therefore, we require the error in the registration to be less than 1 mm, or slightly smaller than the size of the relatively large right coronary artery (cross section 4 ± 2 mm^2 in women) [11].

2 Methods

The goal is to accurately track the epicardial surface over the cardiac cycle. Fig. 1 illustrates how elastic image registration along with 4D imaging can be applied to this problem. The fundamental assumption is that image motion, observed by changing voxel intensities, corresponds accurately to the physical motion of the object.

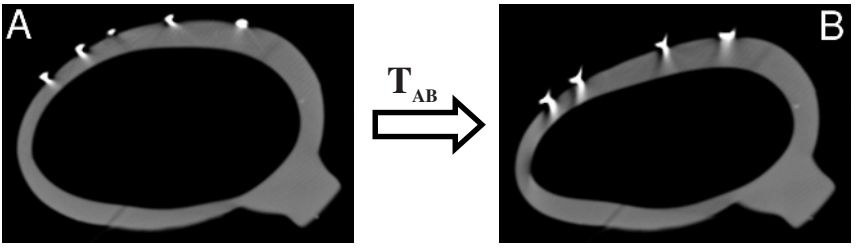

Fig. 1. Slices from CT images of a cardiac phantom, A - end-diastole, B - end-systole. Registering A to B produces transformation T_{AB} that describes the motion between the two images

2.1 Elastic Registration

Our algorithm uses free-form deformations to model the motion of the epicardial surface. First, the source image is overlaid on the target image. In our experience, rigid body pre-registration is not required since differences between two image frames are relatively small. A 3D grid of vectors is then superimposed on the source image to facilitate the elastic deformation. Each vector is optimized separately by minimizing the following cost function using the simplex method of Nelder and Mead [12]:

$$\text{cost}(T_i) = \sum_{V} \left| I_{So}(T_i) - I_{Ta} \right| + \alpha \cdot BE(T_{SoTa}) \; . \tag{1}$$

where T_i is the current vector being tested, T_{SoTa} is the complete transformation from source to target (composed of all T_i), V is the sub-volume of interest surrounding the current vector being optimized, $I_{So}(T_i)$ is the voxel intensity in the source image after translation by T_i, I_{Ta} is the voxel intensity in the target image, and α is the coefficient used to control the cost attributed to the bending energy (BE) of the vector field. The first term is the sum of absolute differences (SAD) between source and target sub-volumes. SAD measures image misalignment, and has previously been used in serial image registration [13] because ideally, serial images differ only by noise and location of features. In addition, the SAD calculation is simple, fast, and can easily take advantage of parallel processing. The second term, calculated using the 3D bending energy definition in [14], ensures that the vector field transformation is smooth.

In order to reduce optimization errors, the algorithm progresses through three stages with increasing vector field density (21 mm^3 of image volume per vector, then 14 mm^3, and finally 7 mm^3). 7 mm^3 was the finest detail used as it suitably balanced accuracy and computation time. At each stage the vector field is interpolated using a linear, cubic or B-spline method prior to being applied to the source image. Higher order interpolation can be used to further ensure that the transformations are smooth.

2.2 Dynamic Epicardial Surface Model

The epicardial surface model is based on multi-slice, helical CT images obtained using a GE LightSpeed Ultra CT scanner, with retrospective gating. Each 4D dataset consists of ten 3D images over the cardiac cycle. Normal canines were scanned after

injection of iodine contrast agent. The animals were paralyzed and artificially ventilated during the 30-second imaging time.

Generating the epicardial surface model can be divided into two distinct steps. First, a static model is created by manually segmenting the epicardium in the end-diastolic image of a given 4D dataset. The end-diastolic image is chosen because heart motion is minimal during this phase. The binary segmentation is smoothed with a spherical kernel Gaussian filter and then rendered in 3D using the marching cubes algorithm [15]. Fig. 2 shows an example of a typical 3D epicardial surface model at end-diastole.

To animate the model, we elastically registered a 4D image of a given subject as illustrated in Fig. 3. The vector field transformations, T_{01} through T_{09}, were applied to the end-diastolic, 3D surface using linear, cubic or B-spline interpolation. The resulting surfaces were then displayed sequentially to portray the dynamic model of the epicardial surface.

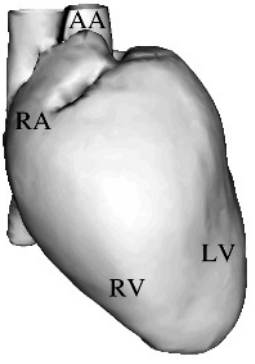

Fig. 2. Epicardial surface model of a canine heart at end-diastole. Labels: left ventricle LV, right ventricle RV, right atrium RA, and ascending aorta AA

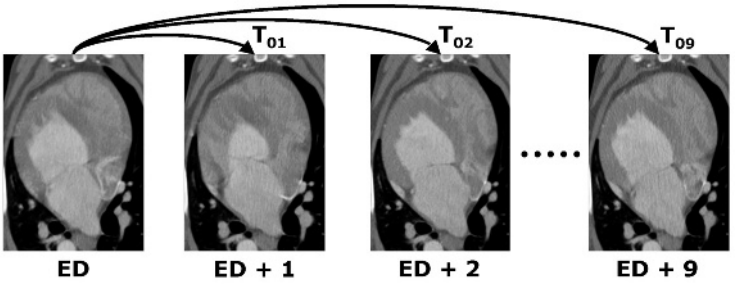

Fig. 3. Measuring cardiac deformation with elastic registration. ED is the end-diastolic image, ED + N is the Nth image in the cardiac cycle. T_{0N} represents the vector field transformation mapping the end-diastole to the Nth time phase image

3 Motion Validation

The ability of our registration algorithm to accurately track the epicardial surface was assessed with experiments on phantom and canine datasets.

3.1 Cardiac Phantom Experiment

Our phantom (Limbs & Things, Bristol, UK) [16] consists of a rubber-like model of a single-chambered heart that rests on a fiberglass "thorax". The phantom is inflated by an air pump, modified to output a TTL trigger to allow ECG-gated imaging. The sur-

face of the phantom was covered with a network of 1 mm-diameter metal wires to simulate the coronary arteries. 1 mm-diameter ball bearings were added in areas not covered by the wire network. The purpose of these modifications was to provide identifiable landmarks for validation (21 in total). A photograph of the phantom with examples of three different landmarks is shown in Fig. 4a.

Seven 3D CT images of the phantom were acquired from end-diastole (N = 0) to end-systole (N = 6) using retrospective ECG gating (images span half of the complete cycle). Iso-surfaces of the coronary network and the ball bearings were easily extracted using marching cubes. Each 3D iso-surface-image pair was rendered with three orthogonal cut planes, as shown in Fig. 4b. Landmarks were located manually by using the mouse to drag a small sphere along the cut planes to the appropriate location on the image. The iso-surface was used as an additional cue to increase the accuracy in finding the landmarks.

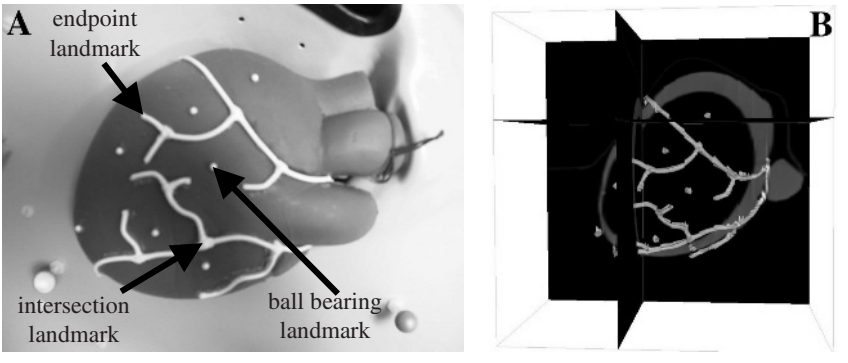

Fig. 4. A – Photograph of the modified cardiac phantom with example landmarks. B – Three orthogonal planes slicing through the end-diastolic CT image; the corresponding wire network iso-surface is overlaid on the image

The error in motion extraction was estimated by comparing the manually selected landmark positions with the corresponding positions obtained from registration. Let LM_N be the set of 21 manually selected landmark locations for an image at time N. We can obtain LA_N (algorithm-derived landmark locations at time N) by registering image 0 to image N, and applying the resulting transformation T_{0N} to LA_0. Table 1 presents the root mean square (RMS) and maximum of the Euclidian distances between corresponding LM and LA landmarks at a given time N. Also shown, is the RMS and maximum distance between LM locations obtained by the same individual on two separate trials (indicates precision in the manual localization step).

Non-zero RMS between LM and LA indicates an overall error in the registration algorithm and in the manual landmark localization step. From Table 1, landmark locations can be selected with a precision of 0.89 ± 0.28 mm, whereas the overall error in motion extraction is 1.14 ± 0.31 mm. Clearly, most of the overall error can be attributed to manually locating landmarks rather than the registration process. Inconsistency in landmark positioning is caused by the large diameter of fiducials (1 mm), metal artefacts in the CT images, and additional motion artefacts in the middle stages of the half-cycle, when the phantom wall is moving at maximum velocity.

Table 1. RMS and maximum of the Euclidian distance for LM_N vs. LA_N and LM_N vs. LM_N. The last row is the mean ± standard deviation over the six landmark set pairs

N	LM vs. LA		LM vs. LM	
	RMS (mm)	Max. Dist. (mm)	RMS (mm)	Max. Dist. (mm)
1	0.58	1.27	0.41	0.81
2	1.04	2.87	0.85	1.98
3	1.32	2.96	1.24	3.33
4	1.48	3.64	1.02	2.55
5	1.23	2.18	0.96	1.61
6	1.20	1.99	0.88	1.92
Mean ± STD	1.14 ± 0.31	-	0.89 ± 0.28	-

3.2 Canine Experiments

For the second experiment we tracked the epicardial surface in 4D images of four normal canine hearts. Because the true cardiac motion was unavailable, we used consistency measurements [17] to validate our algorithm. The schematic in Fig. 5 shows three possible registration loops (each consisting of three propagations) for a series of nine images of a given subject (S_N is the epicardial surface at time N, S'_N is the surface obtained after applying the complete loop of transformations to S_N). The first loop is based on S_0, the manual segmentation of the end-diastolic image, and the S_1 and S_2 loops are initialized by first transforming S_0 with T_{01} and T_{02}. We chose to register images that were three phases apart to approximate the "parallel" approach shown in Fig. 3. For a given loop, we calculated the RMS of the Euclidian distance between corresponding points on S_N and S'_N, effectively estimating the error in the motion derivation procedure over three consecutive propagations. For the error in a single propagation, we divided the RMS by $\sqrt{3}$, assuming that the true error is normally distributed and uncorrelated. Table 2 shows the error in a single propagation averaged over the three possible registration loops for each canine subject.

The estimated error indicates suitable accuracy in motion extraction over the cardiac cycle. In Subject 2 there was an above-average error caused by a metal-like artefact from contrast agent in the right atrium. In Subject 3, contrast agent was evenly distributed, leading to lower error. The above-mentioned artefact is very localized, affecting only a small part of the epicardial surface. Its presence depends on the timing of contrast agent administration and imaging as well as the subject's physiology.

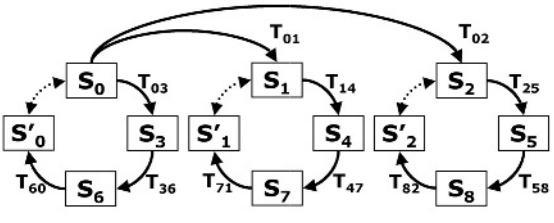

Fig. 5. Registration loops for a 4D dataset composed of nine images used in the validation. S_N is the epicardial surface at time point N (N = 0 is end-diastole)

Table 2. RMS of Euclidian distances between corresponding points on the starting surface and the surface obtained after applying a closed loop of transformations. The RMS is averaged over the three possible loops per subject. Subject 3 was scanned on two different days

Subject	# of Points per Surface	RMS (mm)
1	9037	0.63
2	8658	0.76
3 (day 1)	10853	0.59
3 (day 2)	10276	0.48
Mean ± STD	-	0.61 ± 0.12

4 Conclusions and Future Work

In this paper we presented a method for modeling the dynamic epicardial surface of a potential cardiac intervention patient using elastic image registration. In the phantom experiment, the error in extracted motion was shown to be almost entirely attributable to the error in manually locating the landmarks. The simple geometry of the phantom and the presence of high contrast fiducials in the images contributed to the above average performance. In the canine experiments, the error in extracted motion was estimated to be smaller than the image voxel size. Due to the presence of image artefacts, the true error is probably not uncorrelated as was first assumed. Therefore, the consistency-estimated error is probably an underestimate of the true error. This is not particularity significant because our goal of 1 mm maximum error is much larger than what we observed.

In the validation experiments we concentrated on the epicardial surface *motion* over the cardiac cycle. The accuracy of the epicardial surface itself (manual segmentation) has not been assessed. In the near future we will perform further validation studies using more canine datasets, and eventually, human CT images. The major research direction will be to incorporate subject-specific epicardial models into the virtual environment in order to plan and guide port-access cardiac interventions. When details of the coronary arteries are required, the surface model will be merged with a model of the coronary artery tree, derived from intra-operative 2D angiography. Additional models of the internal structures of the heart will be created using similar registration based methods and will be used to guide intra-chamber procedures.

Acknowledgments. The authors thank Dr. S. Szpala and A. So for the images, Atamai, Inc. and R. Gupta for software and help with code development, A. Costa, Dr. M. Drangova, Dr. M. Wachowiak, J. Moore and Dr. G. Guiraudon for helpful discussions and assistance in writing this manuscript. We also acknowledge funding from the Canadian Institutes of Health Research (MT 14735, MT 11540), Canadian Heart and Stroke Foundation, Ontario Consortium for Image-guided Surgery and Therapy, National Science and Engineering Research Council of Canada, and the University of Western Ontario.

References

1. King, R.C., Reece, T.B., Hurst, J.L., Shockley, K.S., Tribble, C.G., Spotnitz, W.D., Kron, I.L.: Minimally Invasive Coronary Artery Bypass Grafting Decreases Hospital Stay and Cost. Ann. Surg. 225(6) (1997) 805–811
2. Stevens, J.H., Burdon, T.A., Peters, W.S., Siegel, L.C., Pompili, M.F., Vierra, M.A., St. Goar, F.G., Ribakove, G.H., Mitchell, R.S., Reitz, B.A.: Port-Access Coronary Artery Bypass Grafting: A Proposed Surgical Method. J. Thorac. Cardiovasc. Surg. 111 (1996) 567–573
3. Chiu, A., Dey, D., Drangova, M., Boyd, W.D., Peters, T.M.: 3-D Image Guidance for Minimally Invasive Robotic Coronary Artery Bypass (MIRCAB). Heart Surgery Forum, 3(3) (2000) 224–231
4. Gobbi, D.G., Comeau, R.M., Peters, T.M.: Ultrasound/MRI Overlay with Image Warping for Neurosurgery. MICCAI (2000) 106–114
5. Lehmann, G., Habets, D., Holdsworth, D.W., Peters, T.M., Drangova, M.: Simulation of Intra-operative 3D Coronary Angiography for Enhanced Minimally Invasive Robotic Cardiac Intervention. MICCAI (2002) 268–275
6. Sørensen, T.S., Therkildsen, S.V., Makowski, P., Knudsen, J.L., Pedersen, E.M.: A New Virtual Reality Approach for Planning of Cardiac Intervention. Artif. Intell. Med. 22(3) (2001) 193–214
7. Mitchell, S.C., Bosch, J.G., Lelieveldt, B.P.F., van der Geest, R.J., Reiber, J.H.C., Sonka, M.: 3-D Active Appearance Models: Segmentation of Cardiac MR and Ultrasound Images. IEEE Trans. Med. Imag. 21(9) (2002) 1167–1178
8. Declerck, J., Feldmar, J., Ayache, N.: Definition of a four-dimensional continuous planispheric transformation for the tracking and the analysis of left-ventricle motion. Med. Image Anal. 2(2) (1998) 197–213
9. Klein, G.J., Huesman, R.H.: Four-dimensional processing of deformable cardiac PET data. Med. Image Anal. 6 (2002) 29–46
10. Lorenzo-Valdés, M., Sanchez-Ortiz, G.I., Mohiaddin, R., Rueckert, D.: Atlas-Based Segmentation and Tracking of 3D Cardiac MR Images Using Non-rigid Registration. MICCAI (2002) 642–650
11. Kucher, M., Lipp, E., Schwerzmann, M., Zimmerli, M., Allemann, Y., Seiler, C.: Gender differences in coronary artery size per 100 g of left ventricular mass in a population without cardiac disease. Swiss Med. Wkly. 131 (2001) 610–615
12. Nelder, J.A., Mead, R.: A simplex method for function minimization. Computer Journal 7 (1965) 308–313
13. Hill, D.L.G., Batchelor, P.G., Holden, M., Hawkes, D.J.: Medical image registration. Phys. Med. Biol. 46 (2001) R1–R45
14. Rueckert, D., Sonoda, L.I., Hayes, C., Hill, D.L.G., Leach, M.O., Hawkes, D.J.: Nonrigid Registration Using Free-Form Deformations: Application to Breast MR Images. IEEE Trans. Med. Imag. 18(8) (1999) 712–721
15. Lorensen, W.E., Cline, H.E.: Marching Cubes: A High Resolution 3D Surface Construction Algorithm. ACM Comp. Graph. 21(4) (1987) 163–169
16. Stanbridge, R.L., O'Regan, D., Cherian, A., Ramanan, R.: Use of a Pulsatile Beating Heart Model for Training Surgeons in Beating Heart Surgery. Heart Surgery Forum 2(4) (1999) 300–304
17. Holden, M., Hill, D.L.G., Denton, E.R.E., Jarosz, J.M., Cox, T.C.S., Rohlfing, T., Goodey, J., Hawkes, D.J.: Voxel Similarity Measures for 3-D Serial MR Brain Image Registration. IEEE Trans. Med. Imag. 19(2) (2000) 94–102